Mechanical properties of $BaCe_{0.65}Zr_{0.2}Y_{0.15}O_{3-\delta}$ proton-conducting material determined using different nanoindentation methods

Wenyu Zhou[1,2,*], Jürgen Malzbender[1], Fanlin Zeng[1,2], Wendelin Deibert[1], Olivier Guillon[1], Ruth Schwaiger[1], Wilhelm Albert Meulenberg[1,2]

[1]Forschungszentrum Jülich GmbH, Institute of Energy and Climate Research (IEK), 52425 Jülich, Germany

[2]Inorganic Membranes, MESA+ Institute for Nanotechnology, University of Twente, P.O. Box 217, 7500 AE Enschede, The Netherlands

Abstract

Proton-conducting membranes have great potential for applications in proton conducting membrane reactors for the production of commodity chemicals or synthetic fuels as well as for use in solid oxide fuel cells. However, to ensure the long-term structural stability under operation relevant conditions, the mechanical properties of the membrane materials need to be characterized. $BaCe_{0.65}Zr_{0.2}Y_{0.15}O_{3-\delta}$ is of particular interest due to its proven functional properties. In this research work, the mechanical properties of $BaCe_{0.65}Zr_{0.2}Y_{0.15}O_{3-\delta}$ were determined on different length scales using different methods including impulse excitation, indentation testing, and micro-pillar splitting. A detailed microstructural analysis of pillars revealed that irregular results are caused by pores causing crack deflection and complex crack patterns.

*Corresponding author
Email: w.zhou@fz-juelich.de
Tel.: ++49-2461-619399
Fax: ++49-2461-612455

Keywords: Proton conductor; membrane; fracture toughness; mechanical properties; indentation; pillar splitting;

1. Introduction

Already the works by Iwahara et al. [1-3] generated worldwide interest regarding applications related to hydrogen separation at intermediate temperatures. Especially Perovskite-based oxides verified remarkable proton conductivities [4]. In fact, $BaCeO_{3-\delta}$-based materials revealed the highest proton conductivity of all the competing materials under a water-containing atmosphere in the temperature range of 400 - 800 °C [4]. It has been reported that particularly Y and Zr doping can enhance proton conductivity and reduce the problem of poor chemical resistance to H_2O, CO_2 and H_2S, which has long been an unsolved challenge [4-13]. Recent reports have shown that $BaCe_{0.65}Zr_{0.2}Y_{0.15}O_{3-\delta}$ (BCZ20Y15) exhibits both good chemical stability and protonic conductivity [14-17]. BCZ20Y15 has, therefore, been considered as a promising material, which can form, in particular in a composite with $Ce_{0.85}Gd_{0.15}O_{2-\delta}$ (GDC15), a dual-phase proton-conducting membrane with a remarkable H_2 permeation [17].

Under application relevant conditions, a hydrogen separation membrane is operated at intermediate temperatures (600 – 800 °C) and is potentially exposed to high pressure differences across its thickness. Under these conditions, the membrane must maintain its structural and geometrical stability, ideally over an operation period of several years. Hence, the mechanical reliability is of critical concern. Despite the progress regarding conductivity and chemical stability, no systematic investigation of the mechanical properties of BCZ20Y15 has yet been reported. Elastic modulus, hardness and fracture toughness of similar materials, such as $BaCeO_3$- based perovskite materials with different stoichiometries have been reported as ~ 110 GPa, ~ 7 GPa and ~ 1 MPa·√m, respectively [18-20]. These materials usually have the unsolved

problem, though, of forming carbonates in a CO_2-containing environment leading to poor thermochemical stability [15, 21-23].

Elastic modulus, hardness and fracture toughness values are often derived via indentation testing [24-26]. However, for the determination of the elastic modulus, impulse excitation testing is suggested to be more accurate, while deriving of the data from the geometry-specific resonance frequency [27] requires specimens with specific shape and dimensions. Fracture toughness data derived on the basis of conventional indentation testing typically show significant deviations related to specimen preparation and testing as well as analysis procedure, rendering alternative characterization methods very important. As an alternative, the micro-pillar indentation splitting test was recently developed by Sebastiani et al. [28-30] on the basis of sharp indentations into micro-pillars prepared via focused ion beam (FIB) milling. The pillar splitting method was developed with the aim of characterizing local intrinsic fracture toughness on the basis of the critical load values visible as pop-in effects in the load-displacement curves acquired during the indentation process.

Compared to the conventional Vickers-indentation-based fracture toughness test method (VIF) and other currently available microscale mechanical testing methods, e.g., single and double cantilever testing [31], the micro-pillar test method offers several advantages including its ease of application. Note, post-test measurement of the crack length, a factor that is critical for VIF and highly dependent on the image acquisition, is not necessary [32, 33]. Any potential residual stress, that might be induced by stoichiometric gradients or differences in thermal expansion in the case of a thin film on a substrate, is fully released and do not affect the test if the pillars have an aspect ratio of height to diameter between 1 and 4 [34]. Compared to FIB-machined micro-cantilever fracture geometries, difficulties related to friction coefficient calibration and possible Ga^+ ion implantation at the root of the stress-concentrating notch can be avoided [30, 31]. However, also in the case of pillar-splitting size effects were observed, which were related to the FIB-preparation [34].

Although it is not necessary to determine the crack length, the validity of the splitting experiment needs to be confirmed since inaccuracies in the indenter tip positioning can result in an underestimation of the fracture toughness [34].

In this work, investigations of the mechanical properties of BCZ20Y15 are reported. The study involved testing at different length scales, which yielded consistent results for the elastic modulus and hardness, confirming the overall uniformity of the processed material. The fracture experiments at the macro- and microscales exhibit differences, which can be explained by the presence of pores causing irregular crack patterns.

2. Experimental

BCZ20Y15 samples were prepared by a solid state reaction method (SSR). $BaCO_3$ (99%, Sigma Aldrich), CeO_2 (99.9%, Sigma Aldrich), ZrO_2 (99%, Sigma Aldrich), and Y_2O_3 (99%, Sigma Aldrich) were used as starting materials. In the process, precursor powders were mixed in stoichiometric ratios and ball-milled in ethanol for 24 hours. The resultant mixtures were dried at 80 °C and then calcined at 1300 °C for 5 h in air. In order to obtain powders with a fine and homogeneous grain size, calcined BCZ20Y15 powders were ball-milled (ZrO_2 balls, 3.5 mm diameter, weight ratio powder : balls : ethanol = 1 : 2 : 3) in ethanol for 24 h. Afterwards, the mixtures were dried and sieved through a 160 μm mesh.

Bulk membranes were then uniaxially pressed into a disc shape under a pressure of ~ 20 MPa for 5 minutes to obtain pellets with green density of ~ 60%, and diameter and thickness of ~ 27 mm and ~ 1 mm, respectively. The samples were subsequently sintered at 1500 °C for 5 hours in air with a constant heating / cooling rate of 5 $K \cdot min^{-1}$. 0.5 wt. % NiO (99%, Sigma Aldrich) [17] was added as sintering aid after pre-calcination in order to obtain dense samples.

The crystal structure and phase purity of the sintered samples was characterized using an EMPYREAN (PANalytical) diffractometer with parafocusing Bragg-Brentano geometry, employing a Cu-LFF-tube (40 kV / 40 mA), a BBHD mirror, 0.04 rad soller slits, and a PIXcel3D detector. X-ray diffraction (XRD) patterns were recorded at room temperature using a step scan procedure (0.4 s per step, 0.013 ° per step size) in the 2θ range of 5 – 90 °.

The microstructures and topographies were assessed by a Zeiss SUPRA 50VP field emission scanning electron microscope (SEM, Zeiss Microscopy GmbH, Oberkochen, Germany). Before observations were made, the respective specimen was embedded in epoxy resin, ground sequentially using SiO_2 sandpaper with 400 and 2000 grit size and then polished using 6 µm and 1 µm diamond suspension. The final polishing was conducted using 50 nm colloidal silica polishing suspension. The image analysis software Image J [35] was used to determine the grain size and porosity from the SEM images. An Archimedes method was used to determine the density of the BCZ20Y15 specimens. The theoretical density was taken from Springer database [36].

An impulse excitation test was conducted following the procedures outlined in the ASTM standard [37]. Depth-sensing indentation testing was carried out using a Nano Test Vantage system (MicroMaterials, Ltd., Wrexham, UK) equipped with a diamond Berkovich tip. Elastic modulus and hardness were determined from the load-displacement curves following the procedure developed by Oliver and Pharr [38, 39]. The reduced modulus (E_r) was calculated using:

$$E_r = \frac{\sqrt{\pi} \cdot S}{2 \cdot \beta \cdot \sqrt{A_p(h_c)}} \quad (1)$$

where S is the contact stiffness determined from the unloading slope, β a tip-dependent geometry factor assumed as 1.034 , A_p the projected contact area, and h_c the contact depth at the maximum load P_{max}. The plane strain modulus (E^*) then corresponds to:

$$E^* = \frac{1}{\frac{1}{E_r} - \frac{1-\nu_i^2}{E_i}} \tag{2}$$

where E_i is the elastic modulus and ν_i Poisson's ratio of the diamond indenter tip assuming 1141 GPa and 0.07, respectively. Young's modulus E_{IT} was then calculated from E^* using Poisson's ratio of the sample ν_s, which is typically 0.3 for ceramics, using:

$$E_{IT} = E^* \cdot (1 - \nu_s^2) \tag{3}$$

The hardness H_{IT} was determined from the maximum load and the corresponding contact area:

$$H_{IT} = \frac{P_{max}}{A_p} \tag{4}$$

30 indents were performed at a loading rate of 2 mN/s to the maximum loads of 20 and 200 mN. Both thermal drift and frame compliance corrections were applied. The distance between indents was 15 µm and 90 µm at 20 mN and 200 mN, respectively.

Fracture toughness data were derived using the conventional Vickers-indentation-based fracture toughness method [40] at applied loads of 3 N, 5 N and 10 N and by the micro-pillar indentation splitting test utilizing a Berkovich tip indenter [28-30]. The crack length induced by the Vickers indentation impression was measured immediately after the test to avoid subcritical crack growth effects [41]. The empirical Equation 5, which was developed for the half-penny crack mode, was used to calculate the apparent fracture toughness K_{IC} [42]:

$$K_{IC} = 0.016 \left(\frac{E}{H}\right)^{\frac{1}{2}} \left(\frac{P}{c^{3/2}}\right) \tag{5}$$

where *c* ist the crack length determined from micrographs.

Pillars with nominal diameters of 5 µm, 10 µm and 15 µm were FIB-milled using an Auriga Crossbeam workstation (Zeiss Microscopy GmbH, Oberkochen, Germany) operated at 30 kV, 4 nA. A typical pillar is shown in Figure 1.

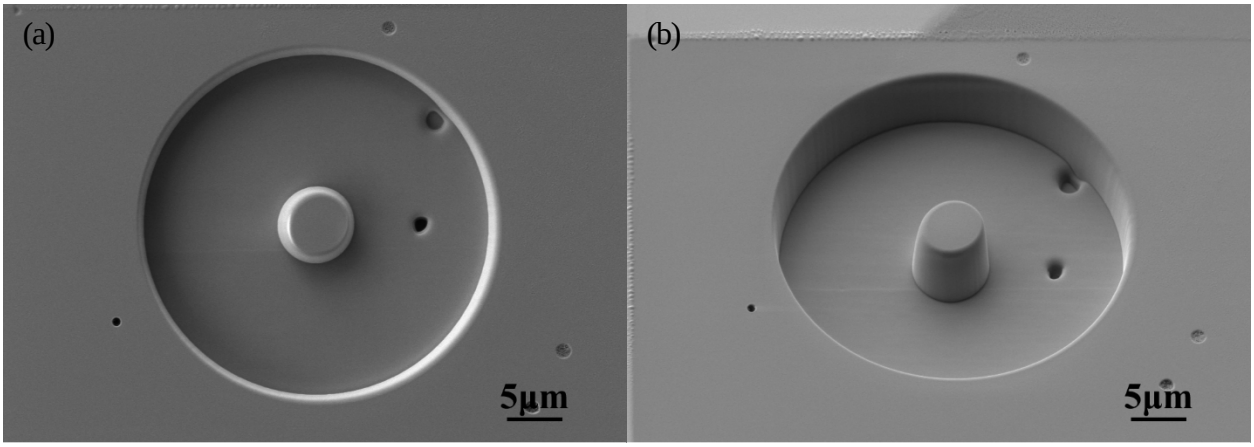

Figure 1. Scanning electron micrographs of a FIB-milled pillar in BCZ20Y15 before testing, (a) top view of a 5 µm pillar, (b) side view of the same pillar, tilt angle 56°.

In total 17 pillars were prepared, six each for the diameters of 10 and 15 µm and five with a nominal diameter of 5 µm. The pillars were not ideal cylinders but rather exhibited a slight taper (approximately 7 degrees) being comparable to values reported in the literature [41]. For the further analysis, the diameter of the pillar top was used [28-30, 41, 43]. Table 1 summarizes the actual pillar diameters, which were used for evaluation of the fracture toughness values.

Table 1. Measured pillar diameters.

	Pillar No.					
Nominal diameter [µm]	A	B	C	D	E	F
5	6.0	6.0	6.0	5.9	5.9	-
10	11.7	11.6	11.5	11.7	11.6	11.6
15	16.2	16.2	15.9	16.1	14.9	15.0

For the sake of clarity, the nominal diameter will be used for the discussion of the results, e.g., 5 µm group. The trench around the pillars was ~ 5 µm wide to allow for observation of cracks on the side surface of the pillars after testing. The load was applied at a loading rate of 2.5 mN/s and pop-ins reflect the pillar splitting.

The fracture toughness values are then calculated using the following equation [30]:

$$K_{IC} = \gamma \cdot \frac{P_c}{R^{3/2}} \quad (6)$$

where P_c is the critical load at pop-in, γ is a dimensionless coefficient that includes the influence of elastic-plastic properties and R is the radius of the pillar. The coefficient γ (eq. 6) was initially calculated by means of the finite element method [30], while in later works a linear relationship between γ and E / H was derived, which holds as long as $7 \leq E / H \leq 21$ [44, 45]:

$$\gamma = 0.0149 \frac{E}{H} + 0.057 \quad (7)$$

Using this equation along with the experimentally determined elastic modulus and hardness, γ takes a value of ~ 0.32.

3. Results and discussion

The material's crystalline structure was verified by XRD and the mean grain size was ~ 13 µm (Figure 2b). The porosity was less than 1% as estimated based on the SEM micrographs using Image J [35]. The Archimedes density was divided by the theoretical density [36] to obtain the relative density, which was more than 99%, corroborating the result based on the image analysis.

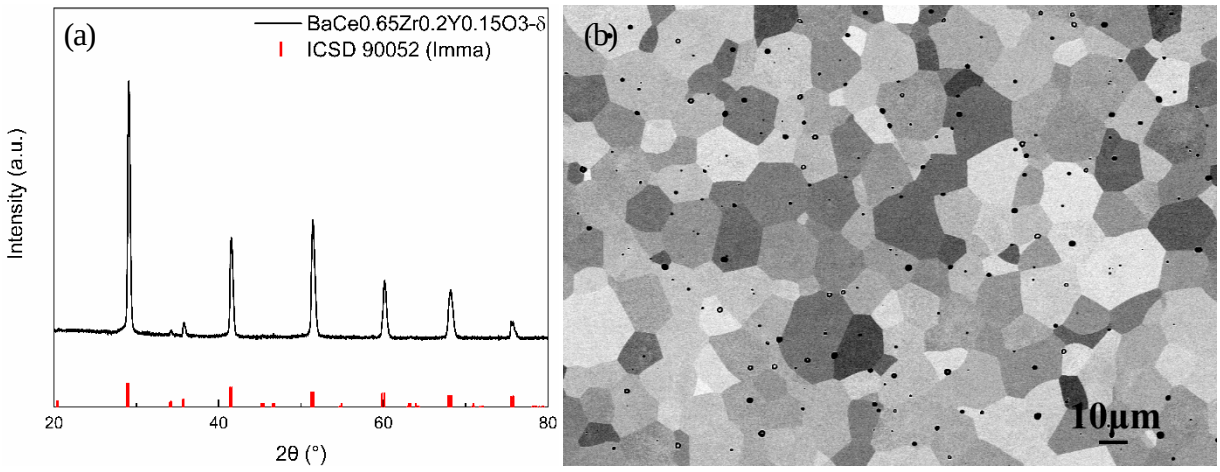

Figure 2. (a) XRD pattern of BCZ20Y15. All peaks are related to BCZ20Y15. (b) SEM image (back-scattered mode) of BCZ20Y15. The contrast differences are due to different crystal orientations and the black spots are pores, which took up less than 1% of the surface area.

The XRD results indicate that, with 0.5 wt% NiO as sintering aid, after sintering at 1500 °C for 5 h, the sample corresponds to single-phase BCZ20Y15 with an orthorhombic structure identified according to the ICSD 90052 (red markers in Figure 2a). Peaks related to NiO were not observed in the XRD pattern, very likely due to the small amount of NiO. Alternatively, NiO might be dissolved in the perovskite lattice or form a BaY_2NiO_5 phase [46]. The detected orthorhombic crystal structure with the space group *Imma* at room temperature for BCZ20Y15 is consistent with that reported by Rebollo et al. [17, 47, 48].

As a global property of BCZ20Y15, the elastic modulus was determined by an impulse excitation test (IET). The frequencies of the first and second natural vibration mode were analyzed from the amplitude-time relationship, yielding ~ 16000 Hz and ~ 28000 Hz, respectively, which served as a basis for the elastic modulus calculation using the relationships given in [37]. The IET results yielded a global elastic modulus of 118 ± 4 GPa, which agrees well with the value determined from the nanoindentation tests. The local elastic modulus of BCZ20Y15 determined from nanoindentation did not show a load dependence and was determined to be 117 ± 6 GPa and 116 ± 2 GPa for 20 mN and 200 mN, respectively. Similarly, no load

effect was observed for the hardness, which corresponded to 6.8 ± 0.6 GPa and 6.4 ± 0.2 GPa, respectively, for the two applied loads (Figure 3).

The good agreement of the modulus values determined from the two independent methods supports the validity of the results and also confirms the high quality of the sample since often elastic modulus values are affected by porosity or material inhomogeneities.

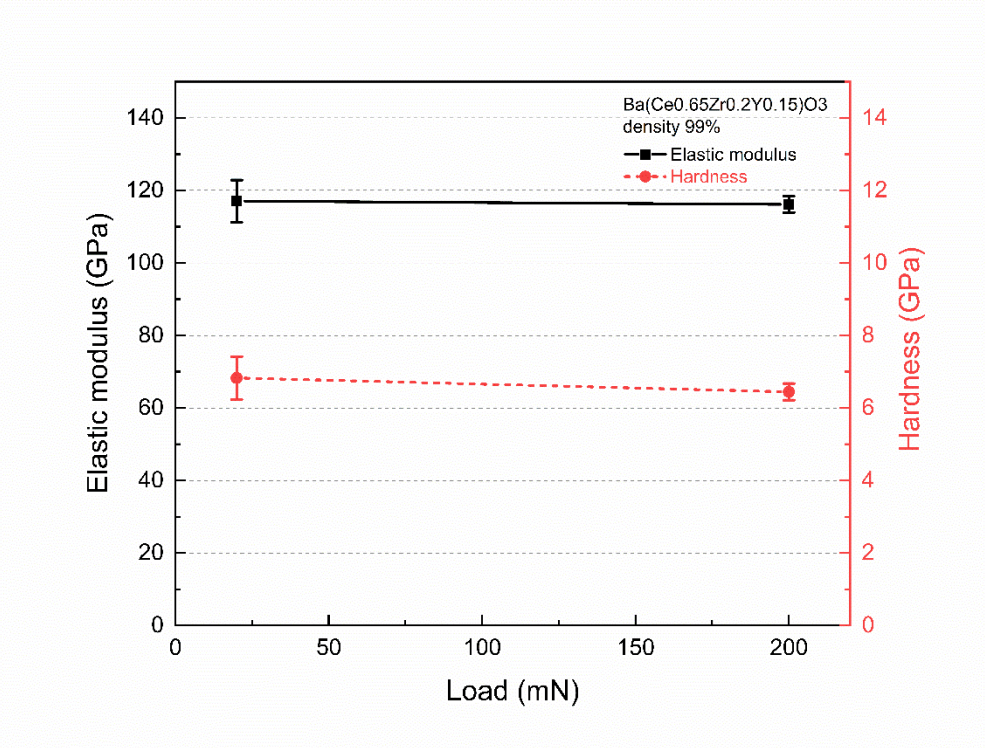

Figure 3. Elastic modulus and hardness of BCZ20Y15 for applied loads of 20 mN and 200 mN.

The fracture toughness was determined from micrographs of Vickers indents and micropillar splitting (Figure 4).

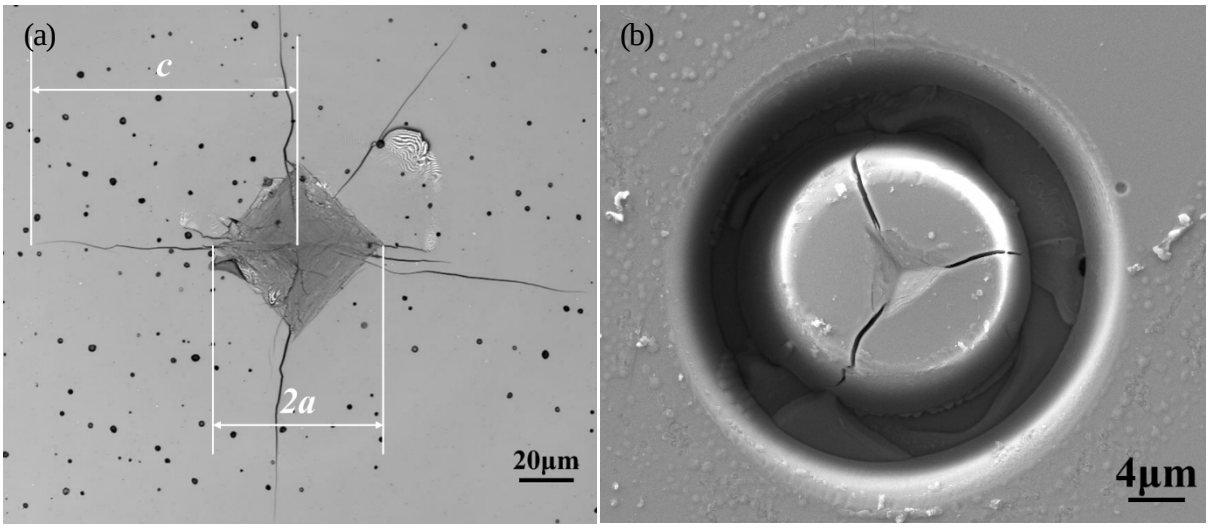

Figure 4. The fracture toughness was determined by the VIF approach and micropillar splitting. (a) Laser scanning microscope micrograph of a Vickers indent into BCZ20Y15 after loading with 10 N. The crack length *c* was used to determine the fracture toughness following the methodology outlined in [42]. (b) FIB machined micropillar with 15 µm diameter after testing showing the typical three-fold symmetry of the crack patterns.

The ratio of *c*/*a* (Fig. 4a), where *c* is the length from the indentation center point to the end of the crack tip and *a* half of the length of the indentation impression diagonal, was verified to be larger than 2.5 for all loads, which usually corresponds to a half-penny crack mode [42]. For the loads of 3, 5, and 10 N, the fracture toughness was determined to be ~ 0.6 MPa·√m (see also Fig. 7 below), with only a slight dependency on the applied load that is within the limits of experimental uncertainty.

Representative load-displacement curves of the pillar splitting tests, along with post-test observation micrographs, are presented in Figure 5. In general, there is good agreement between the curves of the three different pillar sizes and with the loading curve of an indent into the bulk of the sample (Figure 5a), which is critical to ensure the validity of the results [41, 44]. The slight deviation between these curves and the reference curve results is probably a result of thermal drift correction, which could not be performed for the pillar splitting tests due to the fracture preventing the hold period needed upon unloading. However, the thermal drift only affects the displacement measurement, which is not needed to determine the fracture

toughness. The load signal is not affected by thermal fluctuations. The fracture toughness averaged over all pillar tests is 0.93 ± 0.15 MPa·√m, which is in the range typical of ceramics [18, 19, 49].

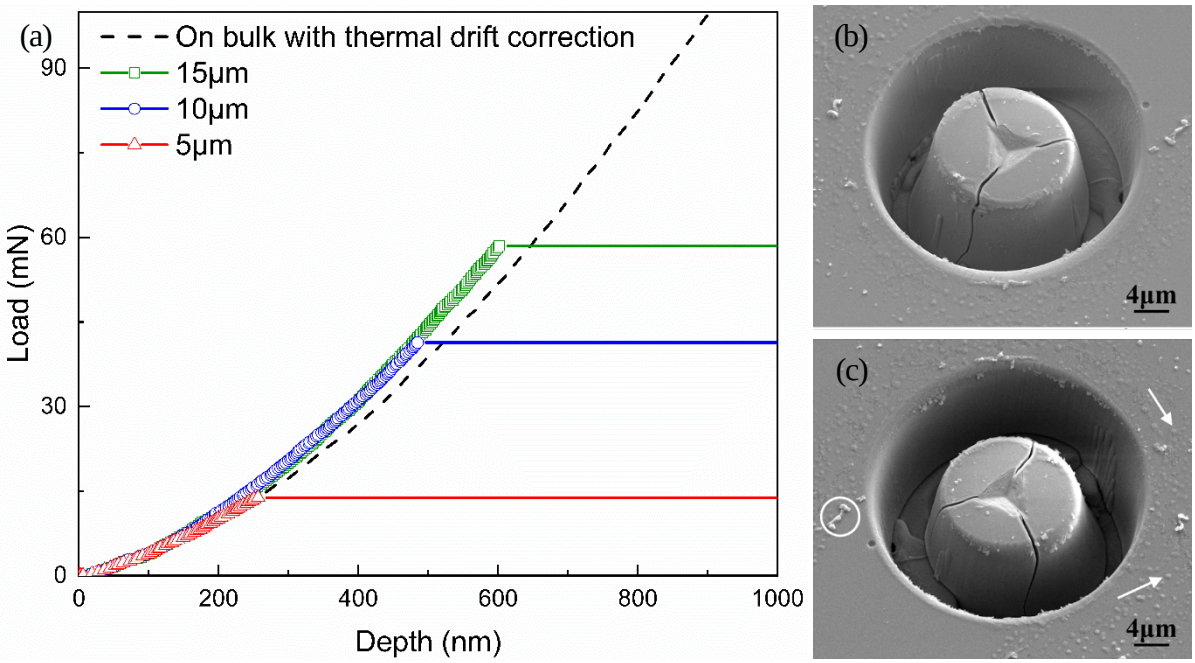

Figure 5. (a) Representative load-displacement curves obtained for the three groups of pillars and on bulk (as reference). (b, c) SEM images a split 15 µm diameter pillar imaged at a tilt angle of 26° and at different rotation angles). Residue on the surface (marked by arrows in c) indicates Ga+ contamination from the FIB preparation. Before imaging in the SEM but post-testing, the sample was coated with Ir, which presents as ribbons on the surface (circle in c).

The indents were all positioned within the central 10% region of the pillars, as exemplified in Figure 4b. Therefore, any unusual behavior related to positioning inaccuracies can be ruled out [34]. All pillars exhibited the typical 3-way splitting (angle of 120° required) with the cracks going straight down to the substrate as shown in Figures 5b and c. No obvious secondary crack or crack deflection was observed. The residue on the surface surrounding the pillars (marked by arrows in Fig. 5c) indicates surface contamination from Ga^+ implantation into the surface resulting from the FIB preparation. In the case of Si, the presence of a ~ 20 – 30 nm thick amorphous layer was observed after FIB preparation, which was reported to have caused a ~ 50% increase of the fracture toughness for single-crystalline Silicon [34]. Our elemental analysis by energy-dispersive X-ray spectroscopy (EDX) revealed that the Ga+ was mainly concentrated at the edge

of pillar (see Figure 6) similar as reported in [41]. Hence, the indentation position appears to be at a sufficiently large distance away from the region affected by the Ga^+.

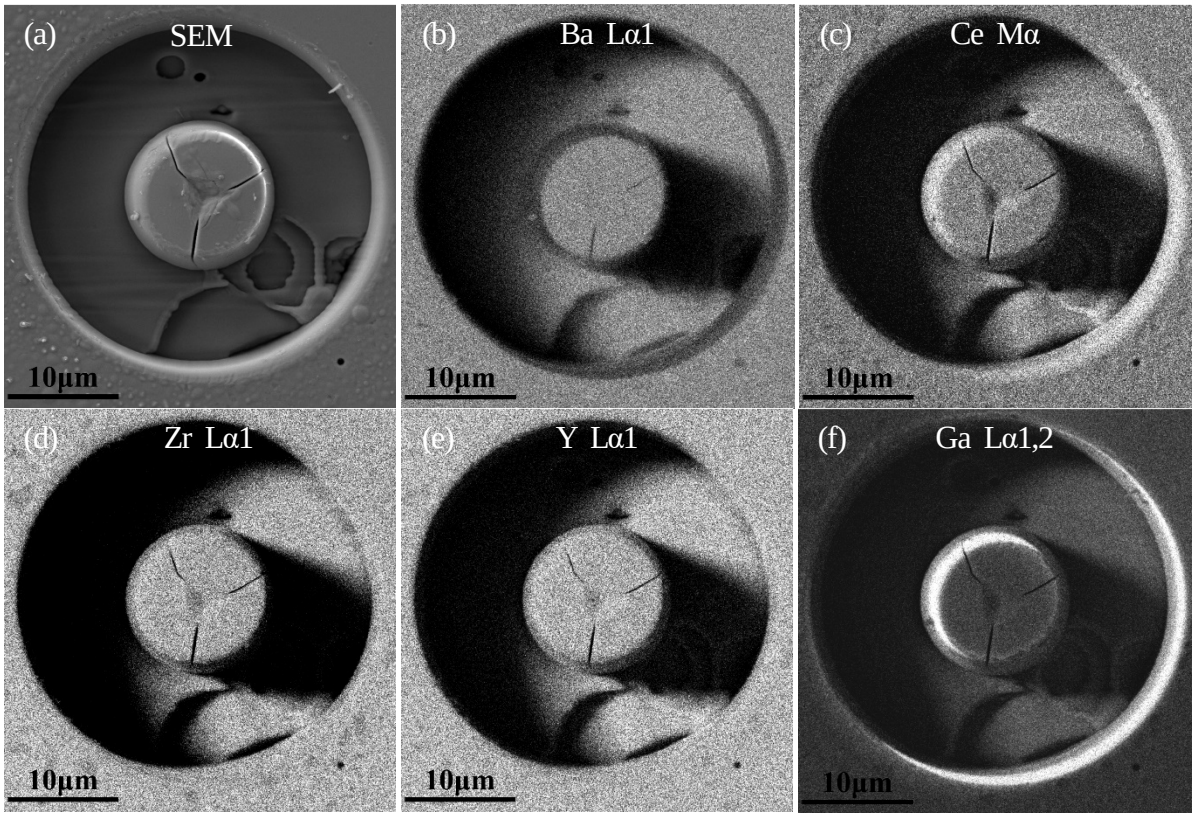

Figure 6. EDX element mapping of a 10 µm pillar after testing showing (a) the SEM micrograph and the elemental distributions (b) Ba, (c) Ce, (d) Zr, (e) Y, (f) Ga. The shadow, which exists in every element mapping, is a result of the topography of the sample surface. Due to the trench surrounding the pillar, no signal from the shadow region can be received by the EDX detector. If an EDX analysis is performed only for selected points on a sample rather than in the form of mappings, the selected location needs to be carefully chosen to avoid erroneous results due to this shadowing effect.

The fracture toughness values of BCZ20Y15 from the different methods are summarized in Figure 7.

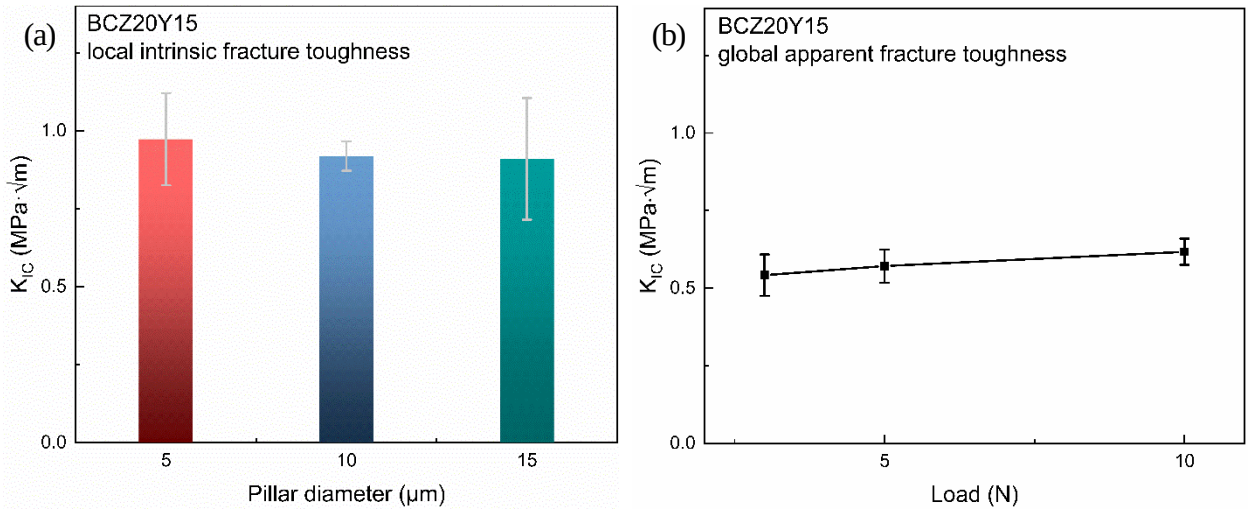

Figure 7. Comparison of the fracture toughness values determined by micropillar splitting and Vickers indentation, which yield values for the local intrinsic (a) and global apparent (b) fracture toughness, respectively.

The fracture toughness determined from pillar splitting is almost independent of the pillar size and therefore unaffected by the FIB preparation. According to the investigation by Lauener et al. [34], the increase in fracture toughness with decreasing pillar size is more pronounced when the pillar diameter is smaller than a critical value of ~ 10 µm. However, in the current case, even the 5 µm pillars showed only a very small increase of the average value compared to the 10 µm and 15 µm pillars. When the error bars are taken into consideration, this difference appears to be negligible.

A clear difference between the fracture toughness values determined by the two methods that probe the material on different length scales can be seen. The global values based on Vickers indentation are significantly lower than the local ones determined from micropillar splitting. R-curve behavior as basis of the difference obtained between these two methods is ruled out since within the range of pillar sizes (micro-pillar test) and applied loads (VIF), within each individual test method, no difference was observed. The BCZ20Y15 is isotropic and homogeneous, and no differences are expected. Therefore, the fracture patterns were investigated in more detail. As already indicated in Figure 4a, the crack paths appear irregular indicating that the VIF results should be viewed as an estimate. A series of Vickers impressions with a load

of 1 N was placed along a line and the BCZ20Y15 sample was split manually to assess the crack patterns underneath the impressions (Figure 8).

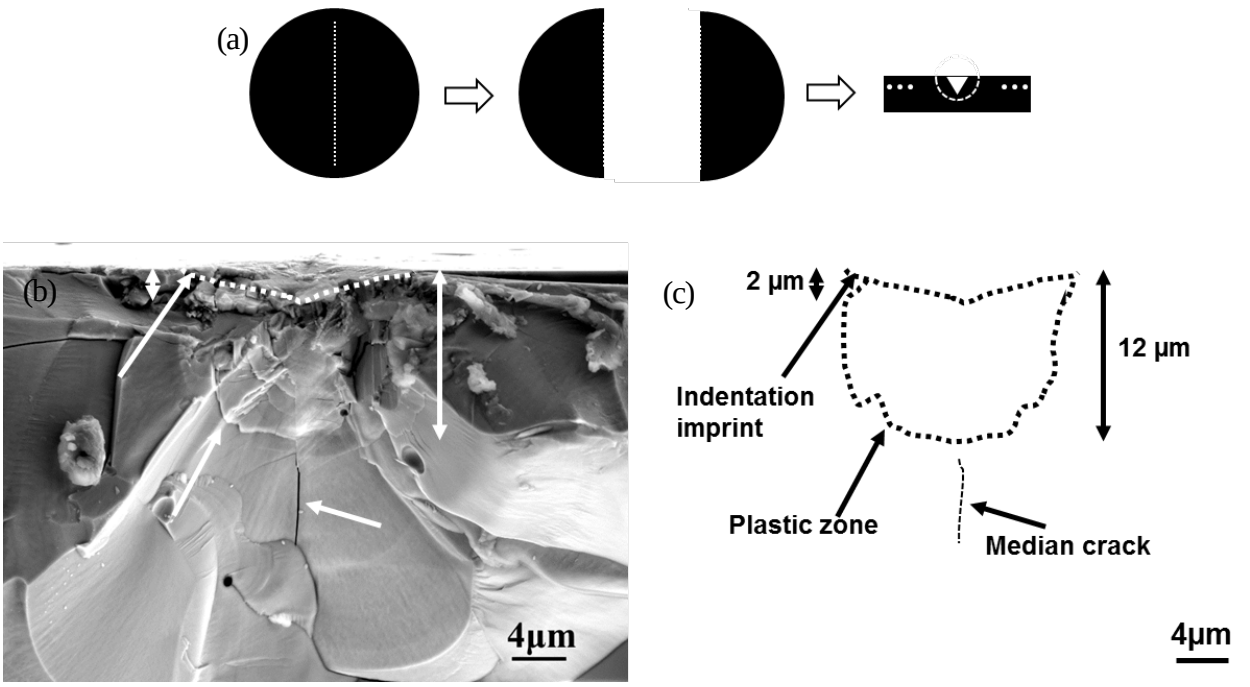

Figure 8. The crack mode was investigated by characterization of the cross section underneath Vickers impressions. (a) Schematic drawing of the preparation procedure. (b) SEM micrograph showing the fracture zone underneath a Vickers impression. (c) Drawing of the characteristic features in the deformed zone.

A clear plastic zone pattern was observed underneath the Vickers impression and an obvious median crack was found, which is a characteristic of the half-penny crack mode [42]. Figure 8 also confirms that the crack propagation mode is trans-granular since no grains or grain boundaries can be observed in the cross-section. The irregular crack patterns, bifurcation and delamination might be responsible for the lower global values.

Since the pillar splitting method only takes into account the necessary energy and load to propagate the cracks, additional secondary cracks, which might form above a critical load, will not influence the derived fracture toughness [41], which is a clear advantage of the pillar splitting method.

We would like to discuss one pillar in more detail, though, since it exhibited a comparably low fracture toughness of ~ 0.7 MPa·√m in contrast to ~ 0.9 MPa·√m averaged over all tested pillars. The pillar had a nominal diameter of 15 µm and exhibited the expected three-fold crack pattern resulting from a well-positioned indent (Figure 9).

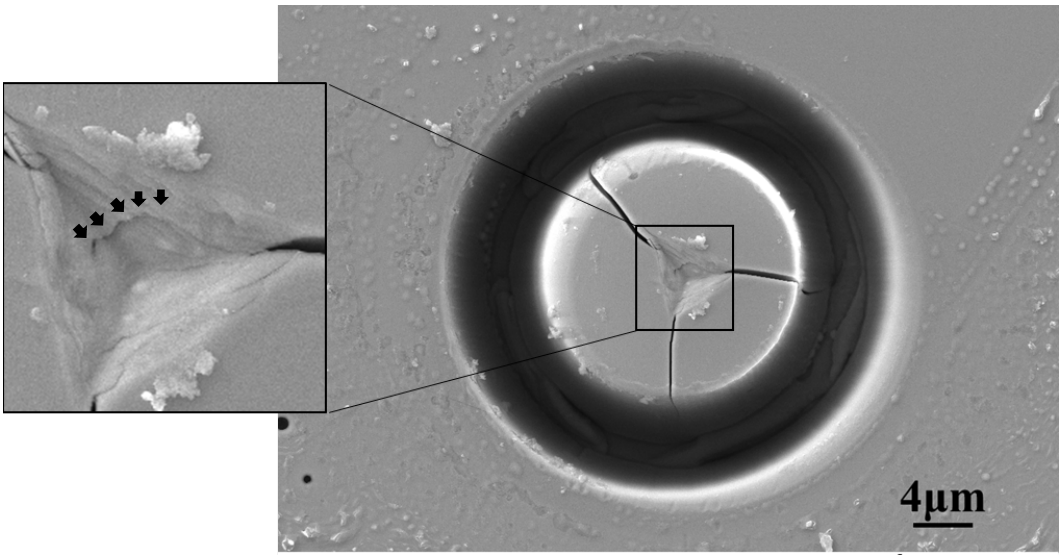

Figure 9. Detailed SEM investigation of the 15 µm pillar No. D (Table 1). The arrows indicate the positions of the crack-like feature inside the indent.

The microstructural analysis revealed a faint crack-like feature inside the indent (marked by arrows in Figure 9), which was apparently caused by pores right underneath the surface as revealed by FIB milling of sequential cross-sections (Figure 10). In the outer part of the pillar (Figure 10a), the crack can clearly be seen (marked as 1 in Figure 10a) with the expected appearance. Crack-like features (marked as 2 in Figure 10a) are curtaining artifacts resulting from the FIB preparation. Towards the center, a more varied pattern is observed. The cross-section through the center of the pillar (Figure 10b), exhibits a well-defined plastic zone (3 in Figure 10b) and a median crack directly underneath the plastic zone (4 in Figure 10b). This observation is in consistent with the expected half-penny crack mode for a Vickers-indentation-based

fracture mechanism [42]. Based on the theory developed by Lawn et al. [50], the initial crack nucleation location for this crack type should be a median crack starting at the region edge of the plastic zone. In general, no crack should be observed in the plastic zone, which is also the case in the current study. However, in the high magnification micrograph in Figure 10c, a round crack-like feature in the surface (5 in Figure 10c) can be seen, which likely is the trace of a pore collapsed during the indentation test but likely having caused crack deflection resulting in a lower fracture toughness value. Evidence for crack deflection at pores can be observed at the bottom of a pillar cross-section (6 in Figure 10d). While the pillar splitting is affected less by inhomogeneities in the volume of the material, pores close to the surface can reduce the value of the fracture toughness determined and, in general, the surface of the pillars needs to be inspected.

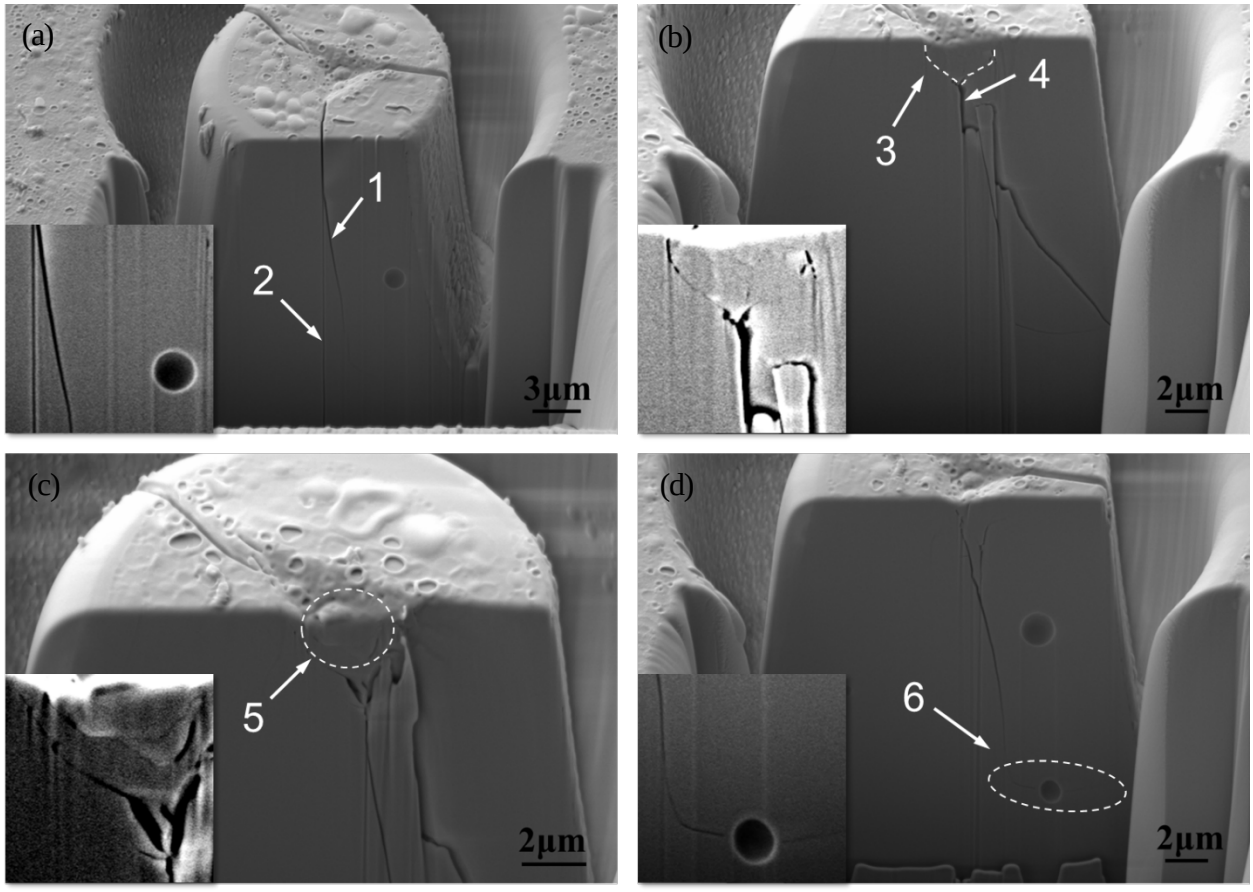

Figure 10. SEM micrographs of sequential FIB cross sections through the 15 µm diameter pillar D reveal the details of the fracture

process. (a) Cross-section in the outer region with a straight crack (1) and curtaining artifacts (2), (b) cross-section through the center of the pillar showing the plastic zone (3) and the median crack (4), (c) cross-section through the crack-like feature shown in Figure 9 indicating the collapse of a pore (5). (d) pore at the bottom of cross section through the pillar showing clear crack deflection (6). Brightness and contrast of the SEM micrographs were adjusted to emphasize the subtle features of the fracture patterns.

4. Conclusions

In this work, the mechanical properties of the proton conducting ceramic BCZ20Y15 were determined applying different micro and macroscale testing methods. Consistent values of the elastic modulus were determined on different length scales corroborating the validity of the values determined. The hardness determined using different maximum loads did not show a dependence on the depth, which reflects the high quality and homogeneity of the material tested. The values of approximately 120 GPa and 7 GPa for the elastic modulus and the hardness, respectively, are in a range typical of ceramic materials and comparable to the properties of similar materials used as transport membranes [18-20]. The local intrinsic fracture toughness determined by micropillar splitting yielded higher values than the Vickers indentation based analysis, which probes a larger volume of the material. A detailed microstructural analysis clearly revealed the effect of pores and crack deflection, which reduces the determined fracture toughness. The VIF based apparent fracture toughness represents a lower estimate due to irregular crack patterns, bifurcation and delamination affecting the derived global values.

BCZ20Y15 appears to be suitable for further studies related to its application relevant properties. In addition to permeation and long-term chemical as well as operational stability, the long-term deformation behavior at elevated temperatures and failure probabilities as well as

subcritical crack growth are of particular interest. In addition, potential stoichiometric changes, degradation effects, and the interplay with mechanical characteristics will have to be studied.

Acknowledgements

This work was supported by the China Scholarship Council (CSC). The authors would also like to especially thank Dr. E. Wessel, Dr. D. Grüner, Mr. M. Ziegner and Ms. D. Esser for the microstructural characterization and Prof. M. Krüger and Prof. L. Singheiser for support.

References

[1] H. Iwahara, Technological challenges in the application of proton conducting ceramics, Solid State Ionics 77 (1995) 289-298.
[2] H. Iwahara, H. Uchida, K. Morimoto, High Temperature Solid Electrolyte Fuel Cells Using Perovskite-Type Oxide Based on $BaCeO_3$, Journal of the Electrochemical Society 137(2) (1990) 462-465.
[3] H. Iwahara, H. Uchida, K. Ono, K. Ogaki, Proton conduction in sintered oxides based on BaCeO3, Journal of the Electrochemical Society 135(2) (1988) 529-533.
[4] K. Kreuer, Proton-conducting oxides, Annual Review of Materials Research 33(1) (2003) 333-359.
[5] G. Chiodelli, L. Malavasi, C. Tealdi, S. Barison, M. Battagliarin, L. Doubova, M. Fabrizio, C. Mortalo, R. Gerbasi, Role of synthetic route on the transport properties of $BaCe1\text{-}xYxO_3$ proton conductor, Journal of Alloys and Compounds 470(1-2) (2009) 477-485.
[6] E. Fabbri, A. D'Epifanio, E. Di Bartolomeo, S. Licoccia, E. Traversa, Tailoring the chemical stability of Ba $(Ce_{0.8-x}Zr_x)$ $Y_{0.2}O_{3-\delta}$ protonic conductors for intermediate temperature solid oxide fuel cells (IT-SOFCs), Solid State Ionics 179(15-16) (2008) 558-564.
[7] S. Haile, G. Staneff, K. Ryu, Non-stoichiometry, grain boundary transport and chemical stability of proton conducting perovskites, Journal of Materials Science 36(5) (2001) 1149-1160.
[8] J. Li, J.-L. Luo, K.T. Chuang, A.R. Sanger, Chemical stability of Y-doped Ba (Ce, Zr) O_3 perovskites in H_2S-containing H_2, Electrochimica Acta 53(10) (2008) 3701-3707.
[9] A. Magrez, T. Schober, Preparation, sintering, and water incorporation of proton conducting $Ba_{0.99}Zr_{0.8}Y_{0.2}O_{3-\delta}$: comparison between three different synthesis techniques, Solid State Ionics 175(1-4) (2004) 585-588.
[10] S. Stotz, C. Wagner, Die löslichkeit von wasserdampf und wasserstoff in festen oxiden, Berichte der Bunsengesellschaft für physikalische Chemie 70(8) (1966) 781-788.
[11] C.W. Tanner, A.V. Virkar, Instability of $BaCeO_3$ in H_2O-Containing Atmospheres, Journal of The Electrochemical Society 143(4) (1996) 1386-1389.
[12] S. Tao, J.T. Irvine, Conductivity studies of dense yttrium-doped BaZrO3 sintered at 1325 C, Journal of Solid State Chemistry 180(12) (2007) 3493-3503.
[13] L. Yang, S. Wang, K. Blinn, M. Liu, Z. Liu, Z. Cheng, M. Liu, Enhanced sulfur and coking tolerance of a mixed ion conductor for SOFCs: $BaZr_{0.1}Ce_{0.7}Y_{0.2-x}Yb_xO_{3-\delta}$, Science 326(5949) (2009) 126-129.
[14] S. Barison, M. Battagliarin, T. Cavallin, S. Daolio, L. Doubova, M. Fabrizio, C. Mortalo, S. Boldrini, R. Gerbasi, Barium Non-Stoichiometry Role on the Properties of $Ba_{1+x}Ce_{0.65}Zr_{0.20}Y0.15O_{3-\delta}$ Proton Conductors for IT-SOFCs, Fuel cells 8(5) (2008) 360-368.
[15] S. Barison, M. Battagliarin, T. Cavallin, L. Doubova, M. Fabrizio, C. Mortalo, S. Boldrini, L. Malavasi, R. Gerbasi, High conductivity and chemical stability of $BaCe_{1-x-y}Zr_xY_yO_{3-\delta}$ proton conductors prepared by a sol–gel method, Journal of Materials Chemistry 18(42) (2008) 5120-5128.
[16] L. Doubova, S. Barison, S. Boldrini, M. Fabrizio, C. Mortalo, C. Pagura, Conductivity studies of sol-gel prepared $BaCe_{0.85-x}Zr_xY_{0.15}O_{3-\delta}$ solid electrolytes using impedance spectroscopy, Journal of applied electrochemistry 39(11) (2009) 2129-2141.
[17] E. Rebollo, C. Mortalo, S. Escolástico, S. Boldrini, S. Barison, J.M. Serra, M. Fabrizio, Exceptional hydrogen permeation of all-ceramic composite robust membranes based on

$BaCe_{0.65}Zr_{0.20}Y_{0.15}O_{3-\delta}$ and Y-or Gd-doped ceria, Energy & Environmental Science 8(12) (2015) 3675-3686.
[18] Y.-P. Fu, C.-S. Weng, Effect of rare-earth ions doped in $BaCeO_3$ on chemical stability, mechanical properties, and conductivity properties, Ceramics International 40(7) (2014) 10793-10802.
[19] R. Sažinas, C. Bernuy-López, M.A. Einarsrud, T. Grande, Effect of CO_2 Exposure on the Chemical Stability and Mechanical Properties of $BaZrO_3$-Ceramics, Journal of the American Ceramic Society 99(11) (2016) 3685-3695.
[20] Z. Zhang, J. Koppensteiner, W. Schranz, J.B. Betts, A. Migliori, M.A. Carpenter, Microstructure dynamics in orthorhombic perovskites, Physical Review B 82(1) (2010) 014113.
[21] K. Katahira, Y. Kohchi, T. Shimura, H. Iwahara, Protonic conduction in Zr-substituted $BaCeO_3$, Solid State Ionics 138(1-2) (2000) 91-98.
[22] X. Ma, J. Dai, H. Zhang, D.E. Reisner, Protonic conductivity nanostructured ceramic film with improved resistance to carbon dioxide at elevated temperatures, Surface and Coatings Technology 200(5-6) (2005) 1252-1258.
[23] P. Sawant, S. Varma, B. Wani, S. Bharadwaj, Synthesis, stability and conductivity of $BaCe_{0.8-x}Zr_xY_{0.2}O_{3-\delta}$ as electrolyte for proton conducting SOFC, international journal of hydrogen energy 37(4) (2012) 3848-3856.
[24] R.O. Silva, J. Malzbender, F. Schulze-Küppers, S. Baumann, O. Guillon, Mechanical properties and lifetime predictions of dense $SrTi_{1-x}Fe_xO_{3-\delta}$ (x = 0.25, 0.35, 0.5), Journal of the European Ceramic Society 37(7) (2017) 2629-2636.
[25] V. Stournari, W. Deibert, M. Ivanova, C. Krautgasser, R. Bermejo, J. Malzbender, Mechanical properties of tape casted Lanthanum Tungstate for membrane substrate application, Ceramics International 42(14) (2016) 15177-15182.
[26] L. Wang, R. Dou, G. Wang, Y. Li, M. Bai, D. Hall, Y. Chen, A case study of mechanical properties of perovskite-structured $Ba_{0.5}Sr_{0.5}Co_{0.8}Fe_{0.2}O_{3-\delta}$ oxygen transport membrane, Journal of the European Ceramic Society 38(2) (2018) 647-653.
[27] J. Wei, G. Pećanac, J. Malzbender, Review of mechanical characterization methods for ceramics used in energy technologies, Ceramics international 40(10) (2014) 15371-15380.
[28] M. Sebastiani, E. Bemporad, F. Carassiti, N. Schwarzer, Residual stress measurement at the micrometer scale: Focused ion beam (FIB) milling and nanoindentation testing, Philosophical Magazine 91(7-9) (2011) 1121-1136.
[29] M. Sebastiani, C. Eberl, E. Bemporad, G.M. Pharr, Depth-resolved residual stress analysis of thin coatings by a new FIB–DIC method, Materials Science and Engineering: A 528(27) (2011) 7901-7908.
[30] M. Sebastiani, K. Johanns, E.G. Herbert, F. Carassiti, G.M. Pharr, A novel pillar indentation splitting test for measuring fracture toughness of thin ceramic coatings, Philosophical Magazine 95(16-18) (2015) 1928-1944.
[31] M. Sebastiani, K. Johanns, E.G. Herbert, G.M. Pharr, Measurement of fracture toughness by nanoindentation methods: Recent advances and future challenges, Current Opinion in Solid State and Materials Science 19(6) (2015) 324-333.
[32] A. Davydok, B.N. Jaya, O. Robach, O. Ulrich, J.-S. Micha, C. Kirchlechner, Analysis of the full stress tensor in a micropillar: Ability of and difficulties arising during synchrotron based μLaue diffraction, Materials & Design 108 (2016) 68-75.
[33] Q. Liu, A. Roy, V.V. Silberschmidt, Size-dependent crystal plasticity: From micro-pillar compression to bending, Mechanics of Materials 100 (2016) 31-40.

[34] C.M. Lauener, L. Petho, M. Chen, Y. Xiao, J. Michler, J.M. Wheeler, Fracture of Silicon: Influence of rate, positioning accuracy, FIB machining, and elevated temperatures on toughness measured by pillar indentation splitting, Materials & Design 142 (2018) 340-349.
[35] C.A. Schneider, W.S. Rasband, K.W. Eliceiri, NIH Image to ImageJ: 25 years of image analysis, Nature methods 9(7) (2012) 671-675.
[36] https://materials.springer.com/isp/crystallographic/docs/sd_1414391 (the database was accessed on 10.07.2019).
[37] ASTM, E. (1876). Standard test method for dynamic young's modulus, shear modulus, and poisson's ratio by impulse excitation of vibration. Annual Book of ASTM Standards, 3, 1876.
[38] W.C. Oliver, G.M. Pharr, An improved technique for determining hardness and elastic modulus using load and displacement sensing indentation experiments, Journal of materials research 7(6) (1992) 1564-1583.
[39] W.C. Oliver, G.M. Pharr, Measurement of hardness and elastic modulus by instrumented indentation: Advances in understanding and refinements to methodology, Journal of materials research 19(1) (2004) 3-20.
[40] J. Gong, Determining indentation toughness by incorporating true hardness into fracture mechanics equations, Journal of the European Ceramic Society 19(8) (1999) 1585-1592.
[41] A.-N. Wang, J.F. Nonemacher, G. Yan, M. Finsterbusch, J. Malzbender, M. Krüger, Mechanical properties of the solid electrolyte Al-substituted $Li_7La_3Zr_2O_{12}$ (LLZO) by utilizing micro-pillar indentation splitting test, Journal of the European Ceramic Society 38(9) (2018) 3201-3209.
[42] C.B. Ponton, R.D. Rawlings, Vickers indentation fracture toughness test Part 1 Review of literature and formulation of standardised indentation toughness equations, Materials Science and Technology 5(9) (1989) 865-872.
[43] A.M. Korsunsky, M. Sebastiani, E. Bemporad, Residual stress evaluation at the micrometer scale: Analysis of thin coatings by FIB milling and digital image correlation, Surface and Coatings Technology 205(7) (2010) 2393-2403.
[44] M. Ghidelli, M. Sebastiani, K.E. Johanns, G.M. Pharr, Effects of indenter angle on micro‐scale fracture toughness measurement by pillar splitting, Journal of the American Ceramic Society 100(12) (2017) 5731-5738.
[45] A.J. Lunt, G. Mohanty, T.K. Neo, J. Michler, A.M. Korsunsky, Microscale resolution fracture toughness profiling at the zirconia-porcelain interface in dental prostheses, Micro+ Nano Materials, Devices, and Systems, International Society for Optics and Photonics, 2015, p. 96685S.
[46] J. Tong, D. Clark, L. Bernau, A. Subramaniyan, R. O'Hayre, Proton-conducting yttrium-doped barium cerate ceramics synthesized by a cost-effective solid-state reactive sintering method, Solid State Ionics 181(33-34) (2010) 1486-1498.
[47] C. Mortalò, E. Rebollo, S. Escolástico, S. Deambrosis, K. Haas-Santo, M. Rancan, R. Dittmeyer, L. Armelao, M. Fabrizio, Enhanced sulfur tolerance of $BaCe_{0.65}Zr_{0.20}Y_{0.15}O_{3-\delta}$-$Ce_{0.85}Gd_{0.15}O_{2-\delta}$ composite for hydrogen separation membranes, Journal of Membrane Science 564 (2018) 123-132.
[48] C. Mortalò, A. Santoru, C. Pistidda, E. Rebollo, M. Boaro, C. Leonelli, M. Fabrizio, Structural evolution of $BaCe_{0.65}Zr_{0.20}Y_{0.15}O_{3-\delta}$-$Ce_{0.85}Gd_{0.15}O_{2-\delta}$ composite MPEC membrane by in-situ synchrotron XRD analyses, Materials Today Energy 13 (2019) 331-341.
[49] P.-F. Yang, D.-L. Chen, S.-R. Jian, S.-W. Lee, C.-J. Tseng, Mechanical Properties of $Ba_{1x}K_xCe_{0.6}Zr_{0.2}Y_{0.2}O_{3-\delta}$ Oxides by Nanoindentation, Procedia Engineering 79 (2014) 599-605.

[50] B. Lawn, A. Evans, A model for crack initiation in elastic/plastic indentation fields, Journal of Materials Science 12(11) (1977) 2195-2199.